In: AIAA SciTech Forum 2023, 23-27 January 2023, National Harbor, Maryland
DOI: 10.2514/6.2023-1555

Validation case studies of a numerical approach towards optimization of novel fuselage geometries

D.U. Odendaal[1], K.J. Craig[2] and L. Smith[3]
University of Pretoria 1, Pretoria, South Africa

N.E. Mutangara[4], D.S. Sanders[5]
Cranfield University 2, Cranfield, UK

Optimization studies for improved fuselage designs primarily focus on drag reduction. However, when considering an alternative configuration where the stability requirements are assumed to be fulfilled by the main wing, eliminating the need for a tailplane, the fuselage design requirements are reconsidered. This work considers not only the reduction of drag but ensuring a component of lift as well as considering energy recovery potential for propulsion integration. The numerical modelling approach (turbulence model selection, optimization strategy and application of the Power Balance Method) is evaluated through a series of validation cases to determine a level of robustness and certainty. Three cases studies are completed: a 2D, compressible transonic RAE2282 airfoil, a 3D, incompressible low-drag body F-57 and a 3D, compressible body MBB3. The final approach includes a polyhedral mesh and SST *k-ω* turbulence model combined with multi-objective trade-off optimization. Application of the Power Balance Method was validated within 1% for incompressible cases, however for the compressible cases the drag coefficient showed increasing deviation (1.3%) due to residual dissipative quantities.

Nomenclature

C_{LV}	Volume-based lift coefficient		P_K	Kinetic energy inflow rate	W
C_{DV}	Volume-based drag coefficient		P_V	Volumetric power	W
C_F	Skin friction coefficient		P_S	Shaft power	W
C_p	Pressure coefficient		R_e	Reynolds number	
C	Chord length	m	V_∞	Freestream Velocity	m.s^{-1}
D	Drag force	N	X	Streamwise direction	m
$\dot{E}_a$	Axial kinetic deposition rate	W	Z	Vertical direction for airfoil construction	m
$\dot{E}_p$	Wake pressure-defect work rate	W	$\dot{\varepsilon}$	Total energy rate	W
$\dot{E}_v$	Transverse kinetic energy deposition rate	W	$\dot{\varepsilon}_{rec}$	Recoverable exergy rate	W
$\dot{E}_w$	Pressure-work deposition rate	W	$\dot{\varepsilon}_m$	Mechanical energy rate	W
L	Fuselage length	m	ϕ	Dissipation rate	W

[1] M.Eng., Department of Mechanical and Aeronautical Engineering
[2] Ph.D., Department of Mechanical and Aeronautical Engineering
[3] Ph.D., Department of Mechanical and Aeronautical Engineering
[4] M.Eng., Centre for Propulsion and Thermal Power Engineering
[5] Ph.D., Centre for Propulsion and Thermal Power Engineering

I. Introduction

New requirements of the fuselage design could include lifting capabilities and the integration of propulsion in the aftbody Huyssen et al. [1] and Smith et al. [2-3]. Integrating propulsion into the fuselage and potential advantages of Boundary Layer Ingestion (BLI) become more compelling in order to reduce fuel emissions. This leads to the Power Balance Method (PBM) developed by Drela [4] in order to redefine the performance measurements of an aircraft with integrated propulsion, by measuring the mechanical flow power and change in kinetic energy rates.

Previous studies [5-9] considered integrated fuselage propulsion systems that were merely included and analysed on fuselage bodies. Other studies have looked at aircraft optimization in order to reduce drag [10-11] but there has not been any work on the detailed and systematic approach and validation thereof in these studies. Using optimization algorithms for aircraft design become more compelling and incorporating PBM into optimization studies can produce aircrafts that are fuel efficient. So far, a low fidelity Aircraft Concept Designs and Trade Studies (TASOPT) [12] was used as the basis of conceptually defining the D8 configuration by optimizing the aircraft aerodynamic performance while evaluating the power balance method for energy recovery purposes.

A numerical modelling approach to optimize a fuselage towards integrating propulsion should include power balance terms as part of the objective function. In order to establish such an approach, a series of stepwise validation cases need to be conducted to ensure a robust and reasonable degree of certainty of the methods that are combined. This paper will consider the approach of turbulent model selection, optimization strategy selection and the application of the PBM to case studies in similar flow conditions. All of these aspects are combined in a separate full fuselage optimization study [13].

II. RAE2822 2D Transonic Validation Case

A. Geometric Model and Mesh Generation

The experimental NASA wind tunnel study [14] on the 2D, compressible RAE2822 airfoil is used to validate the models in the approach. These tests were performed at cryogenic conditions (around -17.6°C) to increase the Reynolds number 6.5 million (based on a chord length of 1m). a Mach number of 0.729, a temperature of 255.56 K, and an angle of attack of 2.31°. Extensive results from these tests are available in the NPARC database [18]. The RAE2822 airfoil is used to validate mesh construction and refinement regions and also to validate turbulence models.

Two computational domains were generated in STAR-CCM+, a polyhedral unstructured mesh structure and a structured mesh which followed Koti [16] method in order to determine which mesh implementation gave the most realistic results. For the rectangular domain, the upstream and downstream domains extend to 10c and 15c, respectively, with a height of 20c. There are five refinement areas employed in the polyhedral meshing domain as defined schematically in Fig. 1. The C-Type domain is split up into five regions. This leads to an inlet radius of 10c, a downstream boundary again being 14c from the trailing edge and a domain height of 20c. The airfoil top and bottom region refinement focused on the leading and trailing edges of the airfoil and used a two-sided hyperbolic cell size growth. Constant cell size was used along with the airfoil shape. Away from the airfoil, one-sided geometrical stretching was used towards the outer boundary of the C-Type domain. Both domains had a boundary layer mesh with a total thickness of 0.003m with 30 prism layers and a stretching factor of 1.1. The domain and mesh constructions with their refinement regions are shown in Fig. 1.

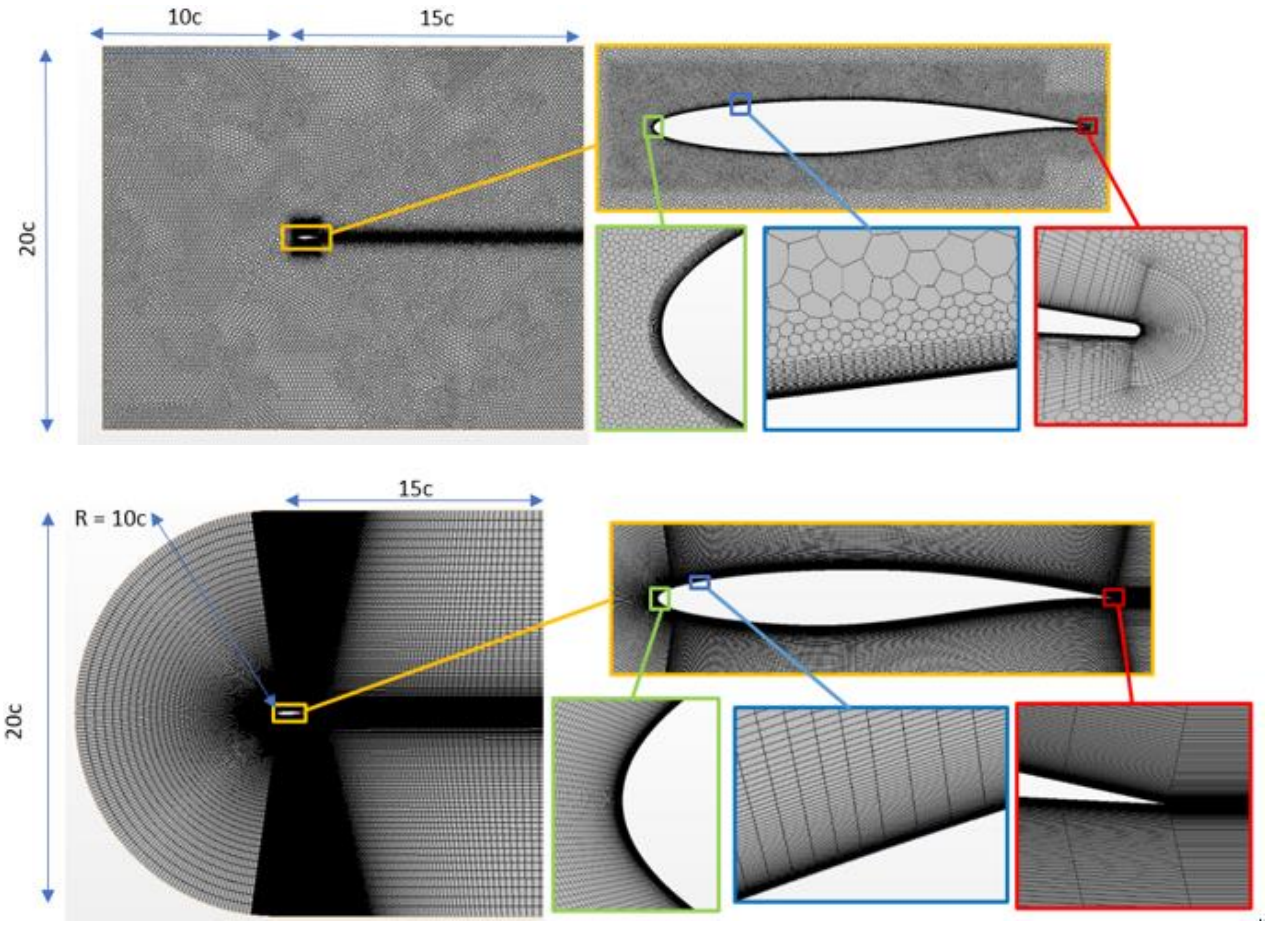

Fig. 1: 2D domain characteristic for a) Unstructured Polyhedral mesh and b) Structured mesh with boundary layer refinement allocations

A mesh independence study was performed for both meshes using the Grid Convergence Index (GCI) method of Roach [17]. Fig. 2 shows the mesh convergence results for the near field lift and drag coefficients that prove that mesh convergence was achieved for both unstructured polyhedral and structured mesh composition. The finest meshes considered contained 359 691 and 362 500 cells for the polyhedral and structured mesh, respectively. Fig. 2 indicates percentage deviations of the CFD results from the experimental reference results which conclude that the finest mesh will be used for the study as it has the smallest deviation from the experimental results.

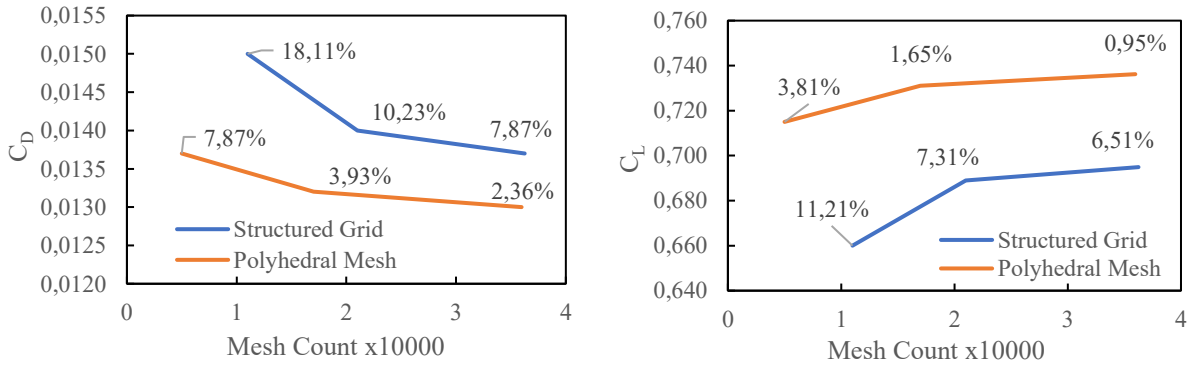

Fig. 2: Mesh related convergence study based on lift and drag coefficient for RAE 2822 for structured and polyhedral mesh

B. Structured Compared to Polyhedral Meshing

Table 1 shows the results of the current work as well as other CFD studies were done by Slater [18] and Gao et al. [19], as compared to Cook et. al [14] experimental results. Gao et al. [19] used an H-type topology structured mesh with a y^+ of less than 0.1, with refinement regions at the leading edge, wake and aft-portion of the airfoil. The Slater [18] CFD study has a C-type mesh with refinement regions around the leading edge, over the airfoil and in the wake. Both simulations used compressible Reynolds-averaged Navier-Stokes equations with the Spalart-Allmaras turbulence model. The current structured and polyhedral mesh was also simulated for compressible Reynolds-averaged Navier-Stokes equations with Spalart-Allmaras turbulence model with ideal gas assumption. Gao et al. [19] results were the closest to the experimental results in terms of drag coefficient while the current polyhedral mesh predicted the lift coefficient the best. In conclusion, the unstructured polyhedral mesh construction paired with refinement regions provided the closest agreement to the experimental values, thus all further simulations will have unstructured polyhedral mesh and similar mesh refinement regions.

Table 1: RAE 2822 experimental values (case 4) test results [14] compared to Slater NASA CFD [18], Gao et al. [19] and polyhedral/structured mesh validation results for lift and drag coefficients.

Mesh	Cell count	y^+	C_L	C_D	Deviation in C_L	Deviation in C_D
Cook et al. [14] Exp.	-	-	0.7433	0.0127	-	-
Slater [18] Num.: Spalart-Allmaras	-	N/A	0.7309	0.0121	1.66%	4.59%
Polyhedral Mesh: Spalart-Allmaras	359691	< 1	0.7362	0.0130	0.95%	2.36%
Structured Mesh: Spalart-Allmaras	362500	< 1	0.6949	0.0137	6.51%	7.87%
Gao et al. [19] Num. Spalart-Allmaras	527468	< 0.1	0.7217	0.0126	2.90%	0.48%

C. Turbulence model selection

The next investigation was on simulations of the steady turbulent transonic flow around the RAE2822 airfoil which is the standard test case used for turbulence modelling. A selection of four turbulence models was used which are best suited for aerodynamic purposes:

- *k-ε* Turbulence model
  - Realizable k-ε turbulence variation
  - Two-Layer approach
  - All y+ treatment
- *k-ω* Turbulence model
  - SST *k-ω* turbulence variation that combines the k-ε with the k-ω
  - Gamma transition
- Spalart-Allmaras Turbulence model (SA)
  - All y+ treatment
- Reynolds Stress Turbulence Model (RST)
  - All y+ treatment
  - Elliptic Blending

The RAE 2822 experimental case 9 [14] was conducted at a free-stream Mach value of M = 0.73 with an angle of attack of $\alpha = 2.79°$ and at a Reynolds number of $6.5 \times 10^{6.}$ Unstructured polyhedral mesh was used for the turbulence model study, which consisted of 362 500 polyhedral cells. The boundary layer consisted of 30 prism layers with a total thickness of 0.003 m. All wall y^+ values for the different turbulence cases are under $y^+ < 1$. Swanson and Rassow [20] used a C-type mesh with refinement regions around the leading edge, over the airfoil and in the wake. The normal mesh spacing at the surface of the finest mesh is approximately $3 \times 10{-}6$, and the maximum surface cell aspect ratio is about 560 with a grid of 1280 x 256. Swanson and Rassow [20] used compressible Reynolds-averaged Navier-Stokes equations with Menter SST *k-ω* turbulence model. Table 2 indicates the percentage differences between the different turbulence models and Cook's experimental results.

Table 2: RAE 2822 Case 9 turbulence model validation results for lift and drag coefficients

	C_D	% Deviation	C_L	% Deviation
Cook et al. [14] Exp.	0.0168	0	0.800	0
Hirschel [21] Num.	0.0165	2.08	0.827	2.12
Swanson and Rassow [20] Num.	0.0165	1.78	0.821	2.62
Reynolds Stress Turbulence Model	0.0178	5.95	0.762	4.75
k-ω Turbulence model	0.0179	6.54	0.765	4.38
Spalart-Allmaras Turbulence model	0.0175	4.17	0.776	3.00
SST k-ω Turbulence Model	0.0172	2.38	0.782	2.25

Fig. 3 and Fig. 4 show the pressure coefficient, C_p and friction coefficient, C_f which are compared to Cook's experimental results. The C_p for all turbulence models shows very little variation. The leading-edge pressure peak at $X/C = 0.05$ was not fully captured by any turbulence model. The SA and k-ω SST model are almost identical, but the SST k-ω model acknowledges the small shock wave at the leading edge for the upper and lower surfaces of the airfoil.

The difference between the turbulence models is more noticeable in the skin friction coefficient shown in Fig. 4. The two best-performing models (SA and SST k-ω) show similar results. The RST model shows a large deviation in the wall shear stress prediction, especially in the leading-edge area and the section downstream of the shock. The k-ε model also exhibits deviations in these areas, but to a lesser extent. Given these results, the RST and k-ε models will not be used for further simulations. Based on the results shown in Table 2, Fig 3 and 4, SA and SST k-ω turbulence models provided the best results in comparison with Cook et al [14] results.

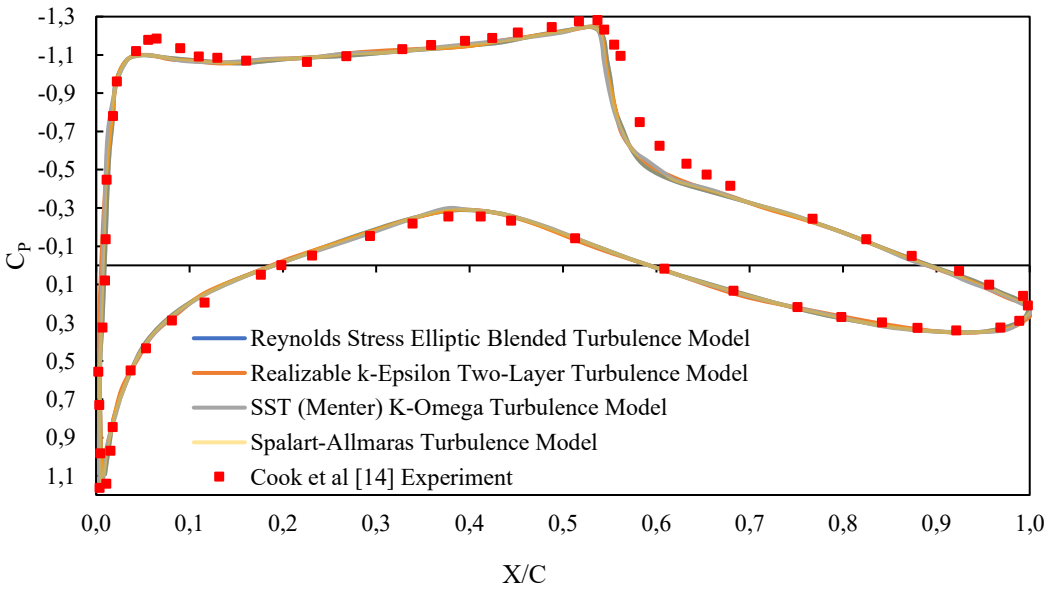

Fig. 3: RAE 2822 Case 9 pressure coefficient distribution over the airfoil surface with enlarged window at shock wave location

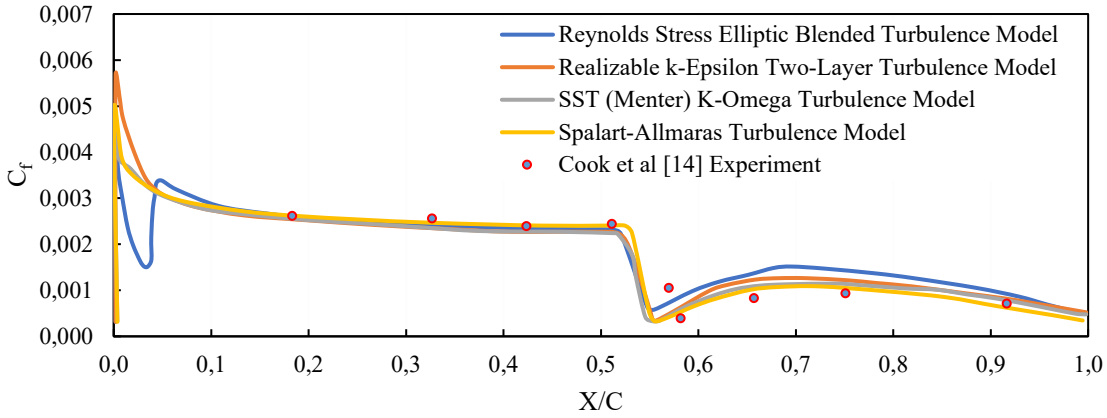

Fig. 4: RAE 2822 Case 9 skin friction coefficient distribution over the airfoil surface for different turbulence models.

III. RAE2822 Case Study for Optimization Strategy Selection

A. Multi-Objective Trade-Off Optimization

The trade-off study needs a parameterised construction of a shape, in this case, an airfoil, in which the dimensions of these parameters can be automatically changed by the SHERPA algorithm [27]. Parameterisation of the airfoil is performed using the PARSEC airfoil method [22]. It uses 11 parameters to design any airfoil as listed and displayed in Fig. 5. The PARSEC method traditionally uses a set of equations to plot hundreds of x and y coordinates [23], but for this case, the PARSEC method is implemented in the STAR-CCM+ CAD program directly instead of a separate code.

The airfoil construction consists of three spline lines shown as 1, 2 and 3 in Fig. 5. For spline number 1, the deflection point is constrained on the vertical and horizontal line which represents the apex of the line. The end points of spline 1 are constrained at the Z_{up}-X_{up} and Z_{lo}-X_{lo} points. The nose radius (r_{le}) is used as a tangential constraint to help with the curvature shape of the nose. The upper and lower crest curvature (Z_{XXup} & Z_{XXlo}) is tangentially constrained to spline 1 which is directly constrained to splines 2 and 3. Splines 2 and 3 are tangentially constrained using the trailing-edge wedge angle (B_{TE}) construction lines and vertically constrained to trailing-edge vertical offset (Z_{TE}).

Parameter	Refined Input Range
α*te*	[0.01, 15] deg
β*te*	[0.01, 15] deg
Rle	[0.001, 0.05] m
Xlo	[0.2, 0.5] m
Xup	[0.2, 0.5] m
Zlo	[0.04, 0.1] m
Zup	[0.04, 0.1] m
Zte	[1.0E-6, 0.02] m
Zxxlo	[0.01, 1.0] m
Zxxup	[0.01, 1.0] m

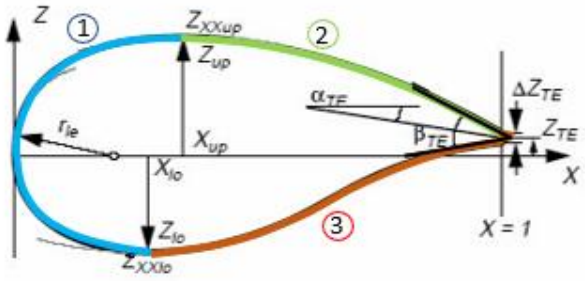

Fig. 5: Defined parameters used to construct an airfoil, known as the PARSEC method.

After the input parameter ranges were refined, a total of 700 designs were conducted with 693 designs feasible, and 7 designs infeasible due to construction divergence. Of the feasible designs, 201 designs (29%) had a performance rating above 1 and 492 designs (71%) were below 1. Fig. 6 shows a performance plot incorporating lift and drag

coefficients for each airfoil design. A Pareto curve forms along the lower part of the graph defining the best designs. This is also an indication of the limit of the optimised airfoil performance in transonic conditions using the PARSEC method.

The corresponding geometries are shown in Fig. 7. These designs are listed in order of ascending lift characteristics. The results are shown in Table 3 all have a performance rating larger than 1. Designs 1 to 7 that show improved aerodynamic performance in comparison to the RAE2822 airfoil has certain characteristics in common.

- All of the optimised airfoils have a slimmer tail due to an average 55.6% decrease in trailing-edge wedge angle (β_{TE}),
- An average 7.94% decrease in upper crest vertical position (Z_{up}) flattens the top surface.
- An average 23.7% decrease in lower crest vertical position (Z_{lo}) which flattens the bottom surface.
- The optimised airfoils increase the total area of high pressure behind the lower crest towards the trailing edge by moving the lower crest horizontal position (X_{lo}) to the front on average by 12.3%.
- The upper crest horizontal position (X_{up}) is moved downstream by an average of 10.2% extending the flat upper surface.
- Additionally, the trailing-edge deflection angle (α_{TE}) is on average increased by 98.3% to aid in retaining the high-pressure region and increasing the camber.
- The leading-edge radius (r_{le}) is on average 25.65% smaller.

The optimised airfoils have more slender shapes than the baseline case with a smaller lower crest vertical position (Z_{lo}) in combination with an overall smaller trailing-edge wedge angle (β_{TE}). The upper crest vertical position (Z_{up}) stays almost the same for all optimised designs but with a higher trailing-edge deflection (α_{TE}). In general, the optimised airfoils have a slender shape with an increase in the camber.

Table 3: Multi-objective parameter inputs with lift and drag coefficient results for best-performing airfoils shown by blue circles in Fig. 6.

Design	RAE 2822	1	2	3	4	5	6	7	8
C_L	0.711	0.712	0.801	0.854	0.938	0.966	1.027	1.091	1.13
C_D	0.018	0.014	0.016	0.017	0.02	0.021	0.024	0.027	0.029
L/D ratio	40.629	49.79	49.444	49.387	46.43	46.225	43.151	41.17	38.672

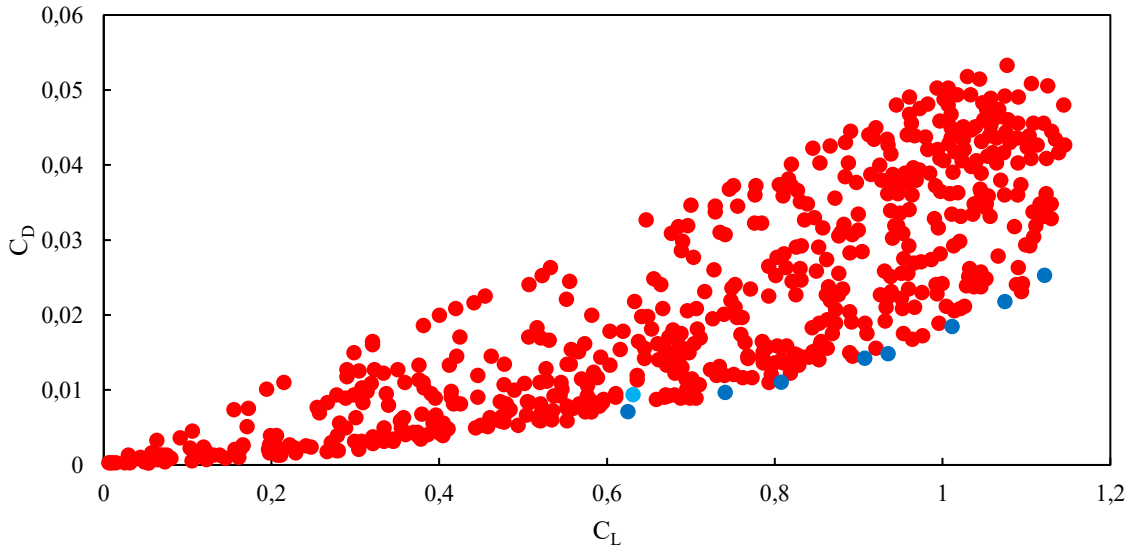

Fig. 6: **All feasible designs' performance characteristics (lift and drag coefficients) are plotted, which shows a clear Pareto line with the best designs. The blue dots indicate the chosen best designs used for analysis.**

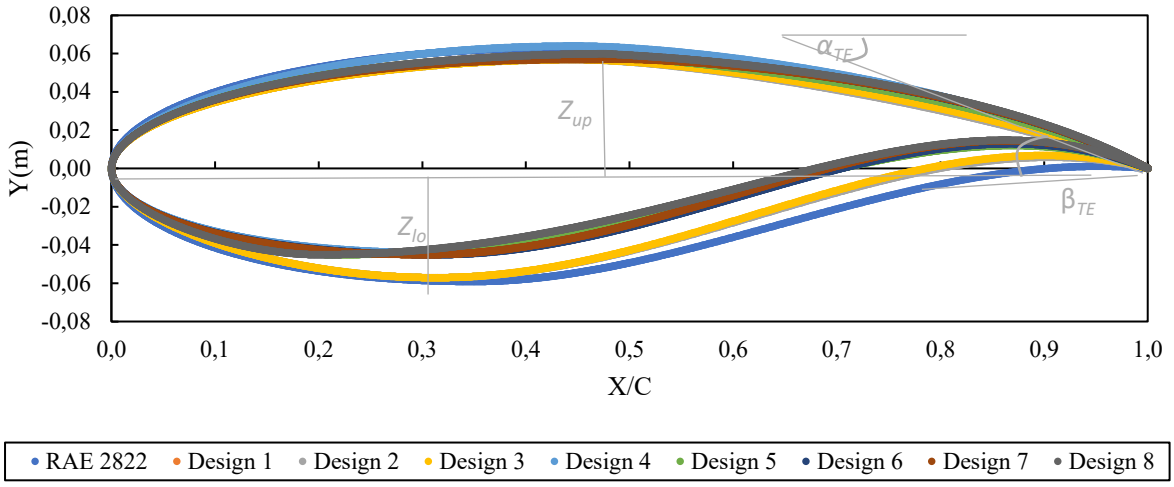

Fig. 7: Multi-Objective optimized airfoil geometries that were selected as shown in Fig. 6.

B. Adjoint Solver Optimization

The implementation of Star-CCM+ Adjoint solver requires an initial simulation with the correct domain, mesh and physics continua. The initial solution must require a high level of convergence as the adjoint solver extracts necessary information to calculate mesh sensitivity. The next step is to assign design variables, known as control point sets, to the geometrical domain where optimization will be performed. Constraints can be implemented regarding what section of the geometry should be optimized by simply applying control point sets to the required surface. These point sets can be implemented in different ways: table form, line, on the part surface or in a lattice. The quantity of design points is controlled by gap distance, where decreasing the gap automatically adds more control points. Any method of control point set can be implemented with an offset from the surface. After the control points are implemented, the adjoint solver will do a mesh sensitivity analysis at each control point.

The expression listed below is implemented to each control point where it calculates mesh sensitivity values and converts them to displacement. Do note that the direction of the mesh sensitivity vector governs the direction of control point displacement. The equation uses a dampening factor (DF) to control the amount of control point displacement.

$$\text{CumulativeMorpherDisplacement} \pm \text{DampeningFactor (DF)} \times \text{MeshSensitivity (MS)}$$

After the sensitivity analysis, the mesh morpher was used. This changes the location of the control points that are attached to the mesh. Moving the control points morphs the mesh around said points which deform the geometry. After the mesh has been morphed, another initial solution is performed where the desired objectives are recalculated. This cycle can be repeated multiple times to acquire desired results.

In this investigation two cases were conducted that covered three basic considerations namely: control point offset distance, control point quantity and dampening factor control. Two control point locations are chosen (Case A (0.01m) and Case B (0.5m) offset) with three sets of the same controlled gap sizes. The gap size between each control point determines the total amount of data capturing nodes which are different for Case A and B. The smallest allowable gap size for this case was 0.001c that increased tenfold for the next simulation. The lift and drag dampening factors (AL DF and AD DF) are kept the same for all simulations. The adjoint optimization parameters are shown in Table 4.

Table 4: Input parameters for a combination of different quantities of control points

Case	Offset	Gap Size	Control Points	Max AD/AL	AL DF	AD DF
A	0.01m	0.001m	1718	3363	1×10^{-7}	1×10^{-7}
	0.01m	0.01m	170	18396	1×10^{-7}	1×10^{-7}
	0.01m	0.1m	15	36250	1×10^{-7}	1×10^{-7}
B	0.5m	0.001m	1773	623.14	1×10^{-7}	1×10^{-7}
	0.5m	0.01m	286	950.38	1×10^{-7}	1×10^{-7}
	0.5m	0.1m	38	2719.0	1×10^{-7}	1×10^{-7}

Before the adjoint optimization process begins, a mesh sensitivity analysis was performed. Fig. 8 shows the 0.001m and 0.1m gap size mesh sensitivity analysis for Cases A and B. The mesh sensitivity analysis shows a force vector for lift (upward/downward arrow) and drag (forward/backward arrow).

Dampening factors (DF) are applied to each control point which acts as the controlling factor for control point displacement. All of the control points are attached to the mesh, moving the control points directly morphs the mesh, which changes the airfoil geometry. Specifying too small a DF causes the control point, with the largest force vector, to be displaced so far that mesh overlapping occurs. For this reason, a sufficiently small DF is specified for each case.

The mesh sensitivity analyses for cases A and B have different AL and AD inflection points as well as different maximum AL and AD locations shown in Fig. 8. For Case A b) the mesh sensitivity has three AL and AD directional inflexion points, the first one is located near the leading edge of the airfoil, the second one is located at the shock wave and the third one is at the lowest crest of the airfoil. This is because the data capturing control points are located close to the surface of the airfoil which experiences a rapid change in flow parameters. This influences the lift and drag force and vector direction calculations. For Case A a) the lack of control points resulted in not fully capturing these rapid changes in flow parameters. In general, the Case B mesh sensitivity analysis has a uniform AD and AL force distribution with the same directional inflexion locations in comparison to Case A. This is due to control points located far away from the region of the geometry where there is less change in flow parameters.

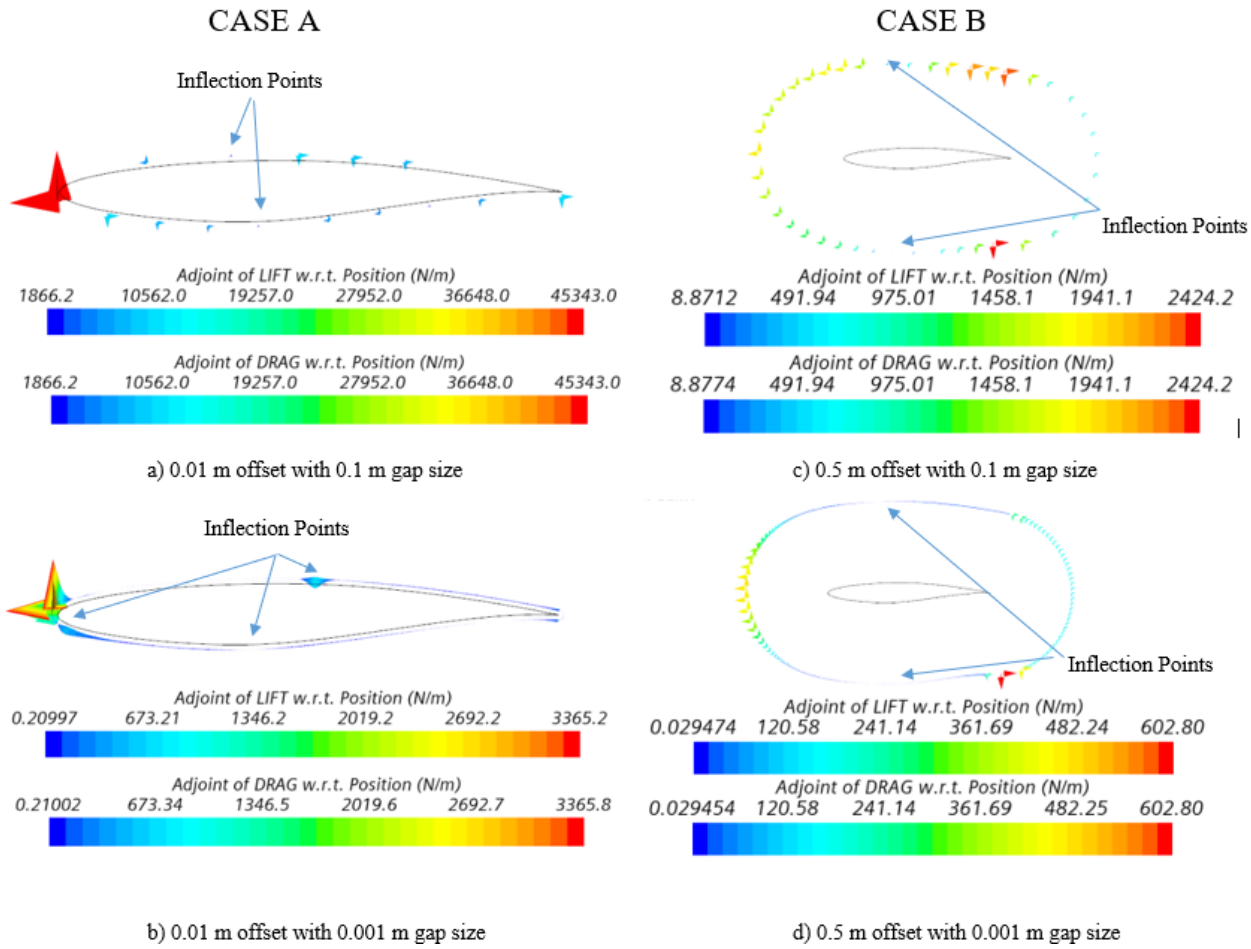

Fig. 8: First mesh sensitivity analysis with different gap sizes for cases A and B.

C. Adjoint Solver Optimization Results

The mesh sensitivity analysis supplies useful information to predict the geometry change after each morphing step. Fig. 9 shows the adjoint optimization results. For Case A, the directional inflexion points and large force vector reside in the same location which is evident in the final airfoils' shapes. The 0.001m and 0.01m gap-size airfoils morphed at the leading edge and at the top crest where the location of the directional inflexion points reside. The result is a drastic

decrease in produced lift and an increase in drag. For the 0.1m gap-size simulation, it morphed a larger area of the airfoil. As shown by the mesh sensitivity analysis, the largest force vectors were at the bottom surface of the leading edge which morphed the leading edge up and inwards. It was also the only optimization from Case A that increased its ability to produce lift. Case B optimized airfoil shapes that all share common traits. The leading edge is raised, lower top crest, lower bottom crest and a lower tail deflection angle. All of the optimised airfoils have increased aerodynamic performance with Case B 0.001m gap size having the highest lift and lowest drag coefficients.

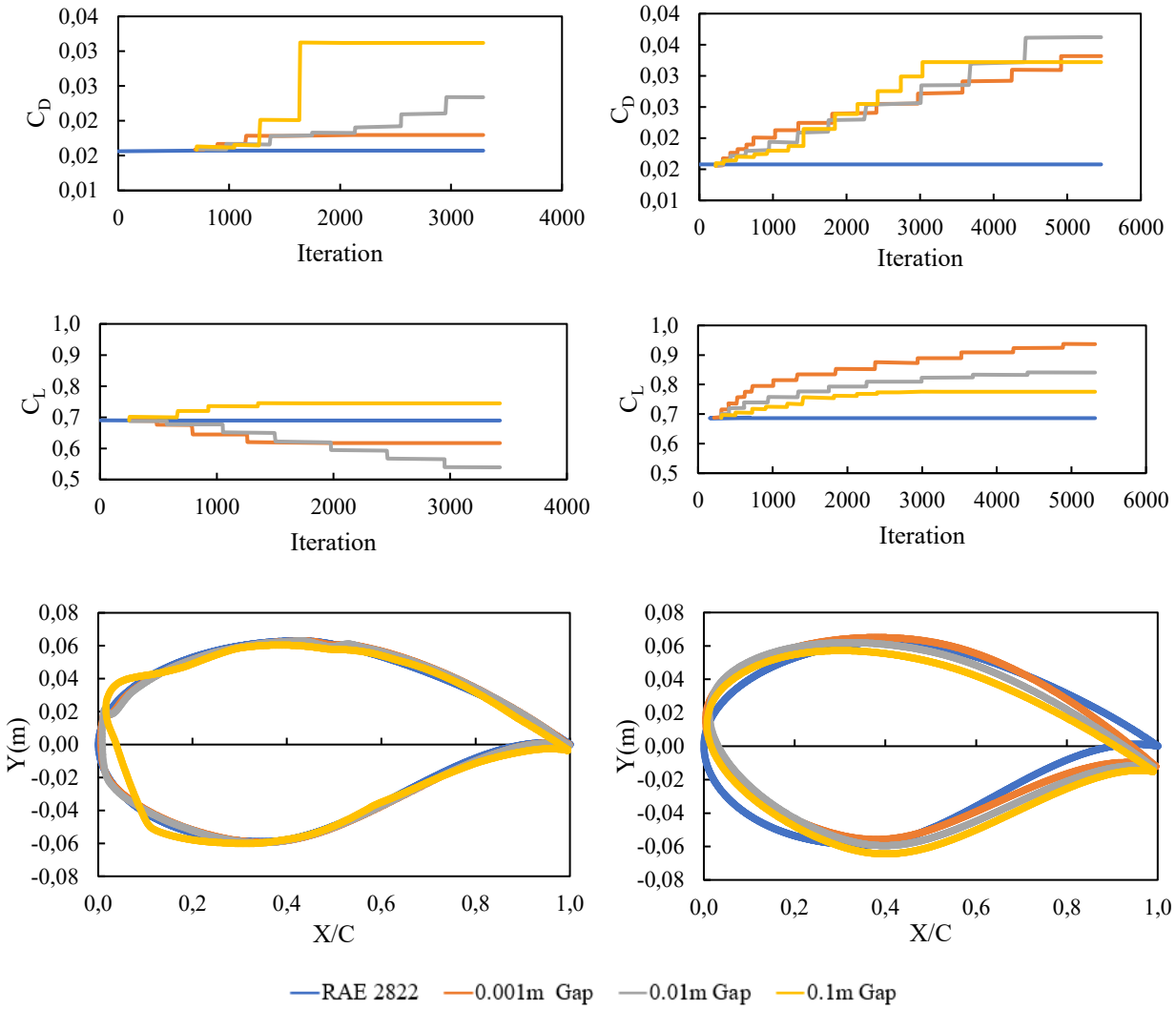

A: 0.01m offset with 0.1m to 0.001m gap size B: 0.5m offset with 0.1m to 0.001m gap size

Fig. 9: Lift and drag coefficient for 0.01m and 0.5m offset cases which correlate with its airfoil geometry

D. Limitations of optimization methods

a. Multi-objective Trade-off Study

Determining the input parameter range proved to be time consuming as there was no prescribed range for any parameter. An initial study had to be performed with guessed input ranges where the parameter range of the best performing airfoils had to be statistically determined and then implemented. A trade-off study requires multiple simulations for the SHERPA algorithm to explore the full domain of different combinations of each parameter input range which is time consuming.

Another limitation of the trade-off study is the CAD model and parameterisation constructions. The PARSEC method consists of 11 parameters that give attachment points for spline lines. Using one spline line for the whole airfoil proved to be difficult as changing a parameter provided an unusable airfoil geometry. This led to implementing three spline lines with constraints to allow flexibility in geometry when parameters change. The PARSEC method leading edge is constrained to one point, which restricts the vertical movement of the leading edge. The trailing edge offset Z_{TE} is set so that it can only move vertically upwards. These constraints limit the freedom of the optimization study.

b. Adjoint Solver

The best implementation for multi-objective adjoint solver optimization is that there should be multiple control points to increase the accuracy of data capturing. The spacing between control points should be evenly spread out to decrease the chances of cells overlapping. Ideally, the mesh sensitivity should display a uniform distribution with a small change in force vector values between neighbouring cells to ensure that the mesh gets morphed uniformly.

The adjoint solver provided numerous limitations in designing capability and controllability. To achieve an optimised geometry, there should be a careful balance between the three basic considerations: control point offset distance, control point quantity and dampening factor control.

- A small amount of control points only gives large values for the mesh sensitivity analysis proceeding to a large geometrical change at that specific control point, which in most cases, negatively impacted the lift and drag performance.
- Having an offset distance close to the airfoil creates multiple inflexion points due to rapid changes in air flow properties. Iterating the morphing process, causes the airfoil to have a wave-like surface due to many inflection points which decreased the performance of the airfoil.
- Each control node is tied to the mesh, so moving the control node, in turn, morphs the mesh. The distance by which a control point moves is determined by the dampening factors. If the dampening factors are too low, the control point will make the mesh overlap itself and terminate the optimization process. Also, morphing the mesh can lead to a deterioration of the quality of the mesh which influences the resulting objective values.

V. Three-Dimensional Validation Cases

A. Introduction

The first 3D validation case is that of the subsonic incompressible flow regime on an F-57 low drag body. Smith et al. [2] and Mutangara et al [5]. both used this case for validation in their numerical studies, providing additional data for comparison. The second validation case considers the transonic compressible flow on a Messerschmitt Bölkow Blohm (MBB) body. The results will be compared to those of Lorenz-Meyer and Auleha's [24] study. These validation cases will lay the foundation for the implementation of the PBM in the CFD study. Firstly, the subsonic F-57 case will be used to validate the PBM by comparing the results to those obtained by Mutangara et al. [5]. The PBM will then be implemented in the transonic MBB shape 3 simulation.

B. Geometric Model and Mesh Generation

The wind tunnel dimensions used for the F-57 low drag body are given as an octagonal cross-section but modified to a square cross-section as mentioned by Smith et al. [2]. The fineness ratio (length/diameter) of the body is 4.75. The body is placed 1L from the inlet surface and 4L from the outlet. The square cross-section has a height and width of 1.25L. The wind tunnel dimensions for the MBB body have a square cross-section of 1.25L width and height. The length of the domain is 3.75L where the body is placed 1.25L from the inlet surface and 2.5L from the outlet surface. The domain dimensions were modified in order to conduct side cylinder variation tests that are used to describe the control volume of the PBM. The new dimensions were 1.6L in height and width with the MBB body placed 1.25L from the inlet surface. The length of the domain is 3.75L. Shape 3 of the MBB experiment is selected with an X_1 value of 0.5L and X_2 value of 0.6875L. The length and diameter of the MBB body are 0.80 m and 0.12 m, respectively.

The computational mesh for both cases is constructed using unstructured polyhedral cells. The subsonic incompressible F-57 simulation had a boundary layer height of 0.33 L consisting of 15 structured cells in order to capture the boundary layer thickening over the surface of the body. For the compressible transonic case on the MBB body, the boundary layer thickness was 0.2L, consisting of 50 structured cells. Both cases resulted in a y^+ value < 1.

There are three common refinements made for both domains, namely the wake region, inner domain and on the surface of the body. Fig. 10 shows the refinement regions for both bodies.

In order to ensure mesh independence, the GCI method is used where three mesh cell sizes were implemented. Fig. 5 shows the results of the mesh independence study based on the C_d values. The final mesh counts for the F-57 and MBB were 1.90 x 10^6 and 1.42 x 10^7, respectively. It shows that the finest mesh refinement deviation in C_d results is satisfactory.

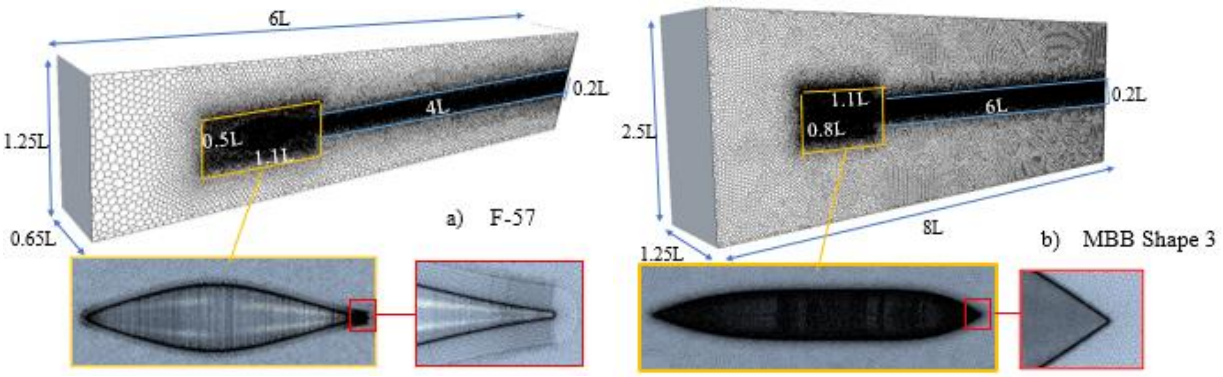

Fig. 10: F57 and MBB shape 3 domain and mesh generation with mesh refinement regions

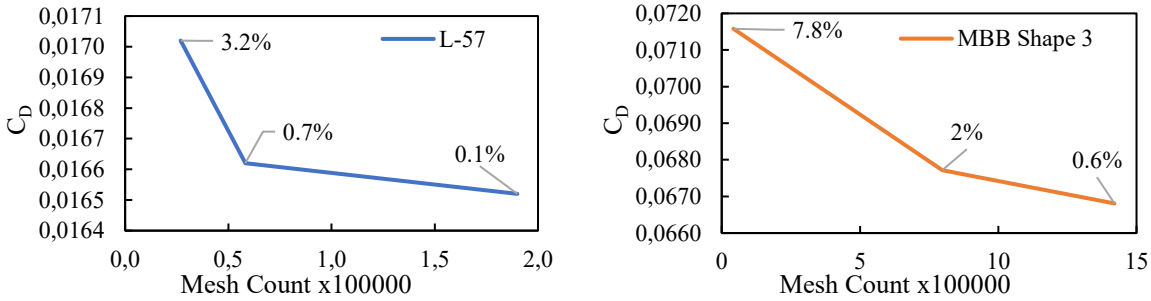

Fig. 11: Mesh-related convergence study of volume-based drag coefficient for an F-57 Low Drag body and an MBB shape 3 body.

C. Incompressible Subsonic 3D Validation Results

The F-57 body was tested at steady incompressible flow at a Reynolds number of 1.2x10^6. The body length from the experiment was used to calculate the constant inlet velocity of 15.24 m/s. The outlet surface was set as an atmospheric pressure outlet and the side walls were set as no-slip wall boundaries. Two simulations were conducted, one using the SST k-ω turbulence model, and the second with a transition model that includes two additional equations, namely for the intermittency (γ) and the Reynolds number based on momentum thickness, Re_θ, called the γ- Re_θ model. A version of the γ-Re_θ model also incorporates turbulence suppression, called the Turbulence Suppression Transition model [2].

The pressure and skin friction coefficient distributions obtained using these two models are compared against experimental results in Fig. 12. In Fig. 12a, the SST k-ω turbulence model and the turbulent suppression transition model gave the same pressure coefficient distribution but for the γ- Re_θ transition model there is a slight deviation at X/L= 0.59 which agrees with the Mutangara et al.[5] and Smith et al. [2] results. Fig. 12b indicates that at the location from X/L = 0.55 to X/L = 0.59 a small separation bubble is modelled not seen in the experimental data or the turbulence suppression model. This is due to the γ- Re_θ transition model simulating the natural transition location further downstream that the experimental transition location at X/L = 0.475.

Patel et al. [25] tripped the boundary layer at X/L = 0.45, which is simulated using the turbulence suppression transition model in a pre-defined region. As a result, the turbulent suppression model shows the best correlation with the experimental results in Fig. 12b), with the γ-Re_θ transition model following the same trend after the natural transition occurs. The inability of the SST k-ω turbulence model to accurately model the skin friction distribution is

because it underpredicts the anisotropy in the turbulence which causes a faster transition to a turbulent boundary layer [26]. Table 5 summarizes the comparison by listing the far-field drag coefficients as compared to Mutangara et al. [5], confirming that the γ- Re_θ model was implemented correctly.

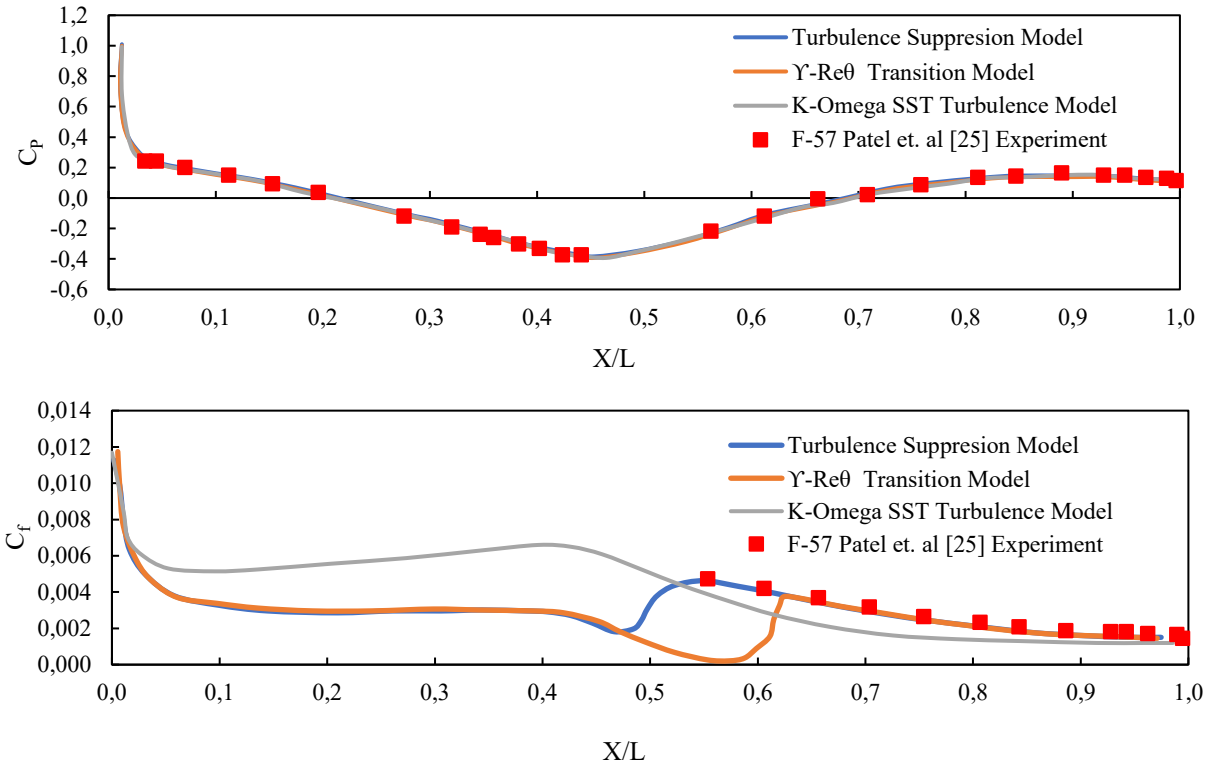

Fig. 12: Pressure and skin friction coefficients for F-57 validation case

Table 5: F-57 validation case results in terms of drag coefficient

Turbulence Model	C_D	Error
Mutangara et al.[5] γ- Re_θ Transition Model	0.0165	N/A
SST k-ω Turbulence Model	0.0195	18.8%
γ-Re_θ Transition Model	0.0165	0%

D. Compressible Transonic 3D Validation Results

The Messerschmitt Bölkow Blohm (MBB) Shape 3 body is simulated with an unstructured polyhedral mesh at Mach = 0.8 with a Reynolds number $10x10^6$. The simulation was set up for coupled compressible flow with ideal gas assumption. The SST *k-ω* turbulence model was used for this validation case. The pressure coefficient distribution over the body is compared to the experimental values of Lorenz-Meyer and Auleha [24] in Fig. 13. There is a good correlation between distribution values with a slight deviation at *X/L* from 0.77 to 0.93. Experimental uncertainty was mentioned in Lorenz-Meyer and Auleha's [24] report due to transonic pressure variations on the centreline. When integrating the normal and shear forces, the experimental and simulated drag coefficients are within 0.6% of the experimental value, confirming the success of the validation shown in Table 6.

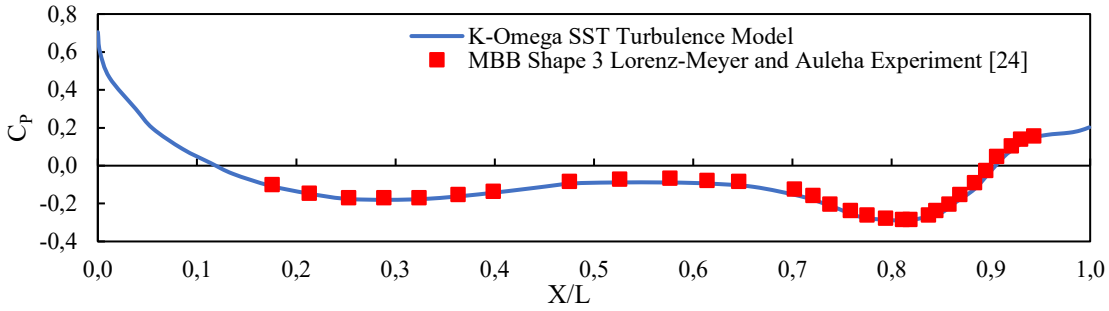

Fig. 13: Pressure coefficient distribution over the MBB shape 3 body

Table 6: MBB shape 3 drag coefficient results

	C_D	Error %
Lorenz-Meyer and Auleha's [24] Exp.	0.0664	N/A
SST k- ω Turbulence Model	0.0668	0.6 %

VI. Power Balance Method Implementation

Mutangara et al. [5] implemented the Drela [4] PBM for the incompressible subsonic F-57 simulation. In this study, the PBM equations and domain definition will be also incorporated into the F-57 simulation for comparison with the Mutangara et al. [5] investigation. After this validation, the PBM will be implemented in the MBB shape 3 transonic compressible simulation using assumptions and recommendations from Drela [4], Sato [9], Sanders and Laskaridis [8].

There are mainly two performance parameters that are relevant for non-propulsion aerodynamic using the PMB coefficients. The Exergy Waste Coefficient (EWC) is used to define the amount of exergy (the maximum useful work which can be extracted from a system as it reversibly comes into equilibrium with its environment) of the control volume compared with the amount of anergy (amount of exergy that is destroyed and not usable). Due to the tested geometries being adiabatic with no heat transfer across any surfaces, the influence of thermal exergy can be neglected, leaving mechanical energy as the main component of the recoverable wake energy.

$$EWC = \frac{\dot{\varepsilon}_{rec}}{DV_\infty} = \frac{\dot{\varepsilon}_m + \dot{\varepsilon}_{th}}{DV_\infty} = \frac{\dot{\varepsilon}_m}{DV_\infty} = \frac{Recoverable\ Exergy}{Total\ Anergy} \tag{1}$$

For transonic conditions, P_V and $\dot{E}_w$ are the non-zero value resulting in fluctuations in $\dot{\varepsilon}_m$ value depending on control volume dimensions. Sanders and Laskaridis [8] used a metric known as a potential for energy recovery (PER) for a performance matric that works out potential recoverable energy based on energy dissipation. Lamprakis et al [28] investigated PBM in transonic compressible flow for axisymmetric body at different Mach numbers and found that increasing the Mach number at a constant Reynold number, $\dot{E}_v, \dot{E}_a, \dot{E}_\rho$ terms increase at the trailing edge but rapidly decay to same value downstream but the (ϕ) and $(-P_V)$ doesn't have the same values further downstream resulting in a net positive compressibility induced residual. P_V has locally reversible and irreversible energy where the irreversible portion is generated predominantly in the boundary layer over the body, with almost no contribution in the free-shear layers of the wake. To give an accurate potential for recoverable energy (PER), integrating over the entire domain, P_{V_∞} cancels out the compressibility induced residual [28]

$$PER = 1 - \frac{\phi - P_{V_\infty}}{\dot{E}_w + E_v + \dot{E}_a + \dot{E}_\rho + \phi - P_V} \tag{2}$$

The main contribution of the PER is that it is useful in plane design because, hypothetically, there may exist two geometrically different bodies with equivalent drag but different PER values. This could, for example, aid in the design of BLI fuselage shaping before the inclusion of the BLI propulsors. A revised EWC equation includes volumetric mechanical power (P_V) and results in a new equation:

$$EWC_{Revised} = \frac{\dot{\varepsilon}_{rec}}{DV_\infty} = \frac{\dot{\varepsilon}_m - P_V + \dot{\varepsilon}_{th}}{DV_\infty} \tag{3}$$

A. Incompressible Subsonic Power Balance Method Validation Results

In order to apply the PBM, a control volume has to be defined in the CFD computational domain. Similar to Mutangara et al. [5], a side "cylinder" is used. Due to the rectangular cross-section being used in the current simulation, the control volume is essentially a cuboid rather than a cylinder, with the Trefftz plane and the inlet plane having rectangular rather than circular cross-sections as in Mutangara et al. [5]. To improve accuracy, the control volume inlet, side, top and bottom locations are located far enough away so that a minimal change in velocity and pressure values from the $P = P_\infty$ and $V = V_\infty$ are present at the control volume boundaries as prescribed by Drela [4]. To judge the effect, the Trefftz plane is translated in the *x*-direction starting from the trailing edge of the body and incrementally shifted downstream by 0.1L.

Drela [4] and Mutangara et al.[5] investigated the variation in the PBM coefficients by moving the Trefftz plane location. The same variations are considered to allow for direct comparison. In terms of the PBM, the assumptions for subsonic incompressible flow are that the mechanical energy outflow disregards any existing shock waves ($\dot{E}_w$) and change in potential energy ($W\dot{h}$) which is only related to the streamwise and transverse kinetic energy disposition rates ($\dot{E}_a, \dot{E}_v$) as well as the pressure defect work rate ($\dot{E}_p$).

$$C_D = C\dot{E}_a + C\dot{E}_v + C\dot{E}_p + C\phi - CP_V$$

Fig. 14 shows the PBM coefficients derived from the current CFD simulation and compared with the Mutangara et al. [5] simulation results. It confirms that the above-mentioned assumptions made while implementing the PBM equations yielded very similar results. The only deviation can be observed in the wake pressure-defect work rate ($C\dot{E}_p$) with a Trefftz plane location near the body, and an overall deviation of 3.8% in the viscous dissipation rate ($C\phi$). The volumetric mechanical power CP_V due to a change in pressure, resulting in a value of zero, which correlates with Drela [4], Sato [9] and Mutangara et al. [5]. In terms of other PBM coefficients, the streamwise kinetic energy rate ($C\dot{E}_a$) and transverse kinetic energy rate ($C\dot{E}_v$) gradually decrease at almost a similar trendline. The wake pressure-defect work ($C\dot{E}_p$) rapidly increases downstream of the body where ($C\dot{E}_v$) and ($C\dot{E}_p$) becomes close to zero at *X/L* = 1.3 at which the streamwise kinetic energy almost entirely contributes to the total mechanical energy. Also, note that the calculated mechanical energy had a small deviation of 0.01% compared with the sum of ($C\dot{E}_a$) ($C\dot{E}_v$) ($C\dot{E}_p$), which is another way to calculate the total mechanical energy.

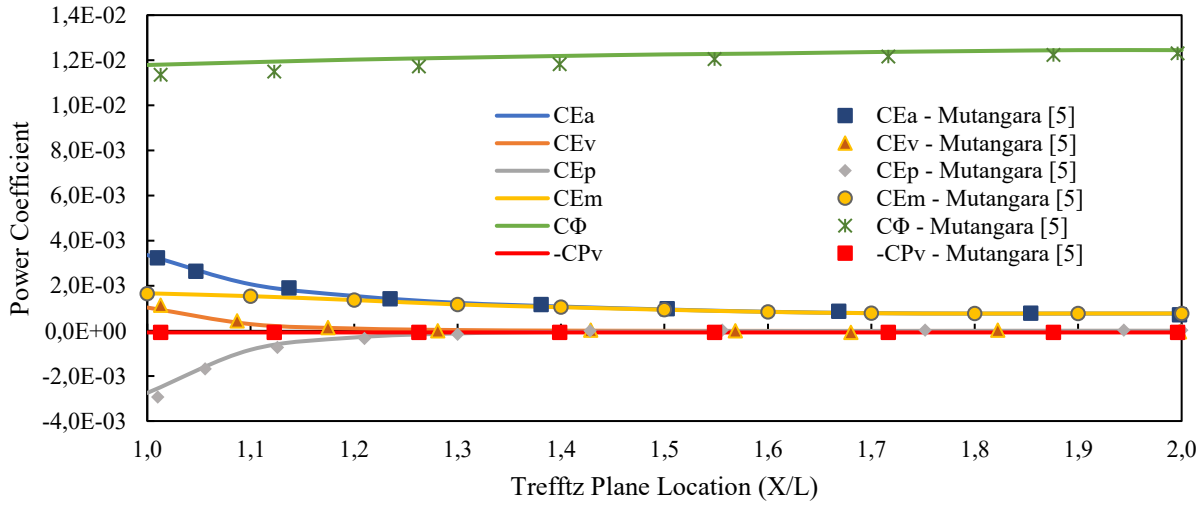

Fig. 14: Comparison of subsonic Power Balance coefficients for F-57 body.

Table 7 shows the results for the drag coefficients calculated using the PBM and using body forces from the simulation. The PBM result was taken one body length downstream from the F-57 body. The near-field drag coefficient and the far-field drag coefficient had a deviation of 0.42% from each other, confirming acceptable implementation. The results from Mutangara et al. [5] displayed a 1.9% deviation. The recoverable energy percentage or EWC value was also calculated and compared to that reported in Mutangara et al. [5], as displayed in Fig. 15. A 0.02% deviation is shown. The EWC measure is useful when evaluating the most beneficial location for propulsion integration into the aftbody of the fuselage.

Table 7: F-57 Power Balance Method and momentum-based drag coefficient results.

	Cell Count	Momentum-based C_{Dv}	Difference	Power Balance Method C_{Dv}	Difference	Deviation
Mutangara et al. [5]	$8.7x10^5$	$1.65X10^{-2}$	N/A	1.62×10^{-2}	N/A	3×10^{-4} (1.9%)
Current F-57	$1.90x10^6$	$1.652X10^{-2}$	0.12%	$1.645x10^{-2}$	1.5%	$7x10^{-5}$ (0.423%)

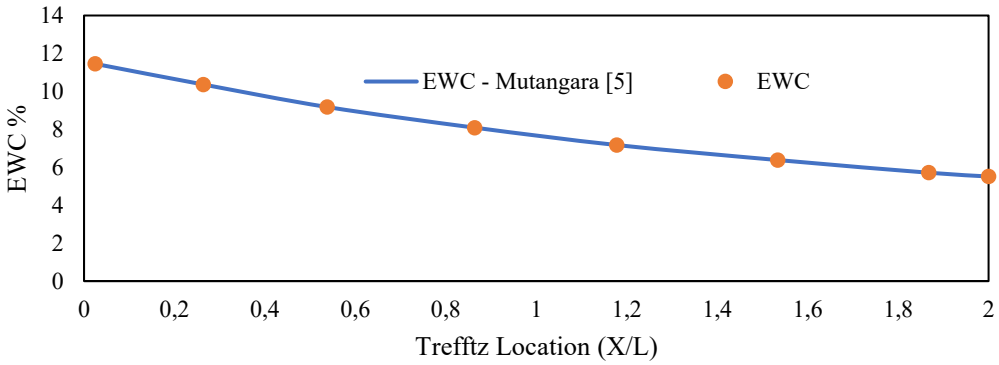

Fig. 15: F-57 recoverable energy percentage from the wake using the EWC performance parameter.

B. Compressible Transonic Power Balance Method Investigation

When considering compressible flow, an additional PBM coefficient, namely ($\dot{E}_w$), is implemented in the CFD simulation. For the incompressible subsonic case, all fluid quantities were recorded in vector form and integrated over all control volume surfaces. For compressible high-velocity cases, the PBM coefficients ($\dot{E}_a$) ($\dot{E}_v$) ($\dot{E}_p$) exits through the Trefftz plane, but with shock wave formation, pressure work ($\dot{E}_w$) is assumed to leave through the side surfaces. For transonic compressible flow, the mechanical energy outflow disregards the change in potential energy ($W\dot{h}$) and is therefore related to the streamwise and transverse kinetic energy disposition rates ($\dot{E}_a$ & $\dot{E}_v$), as well as the pressure defect work rate ($\dot{E}_p$), volumetric mechanical power (P_V) and pressure work ($\dot{E}_w$).

$$C_D = C\dot{E}_a + C\dot{E}_v + C\dot{E}_p + C\dot{E}_w + C\phi - CP_V$$

A variation in control volume dimensions in terms of variation in the Trefftz plane location and side wall location is investigated in order to see if there is a variation in the different PBM coefficients. The main reason for this investigation is to determine the size that the control volume required in order to abide by the assumption made by Drela [4], namely, that pressure work ($\dot{E}_w$) will be zero with a side cylinder located far away from the body. The assumption is that all of the pressure work will dissipate into the surrounding air and not affect the air near the side cylinder boundary. This assumption is tested with all of the PMB coefficients present. Three cases were considered with a variation of side surface distance while the Trefftz plane is moved incrementally (X/L = 0.1) downstream. The side surface distances consist of $0.5L$, $1L$ and $1.5L$, respectively.

Looking at the power coefficient for all transonic compressible cases in Fig. 16, there is a high energy exchange rate between $C\dot{E}_a + C\dot{E}_v + C\dot{E}_p + C\dot{E}_w$ and P_V, starting immediately at the aftbody, which then evens out at a third fuselage length downstream. $C\dot{E}_w$ is marginally nonzero for the $0.5L$ side wall distance because there is some pressure

disturbance at the side control volume due to the shock wave formation, violating the assumption noted above. $C\dot{E}_w$ becomes zero at $1L$ and $1.5L$ sidewall distance, which means that based on this study, the control volume sidewalls should be located at least $1L$ away from the MBB shape 3 body.

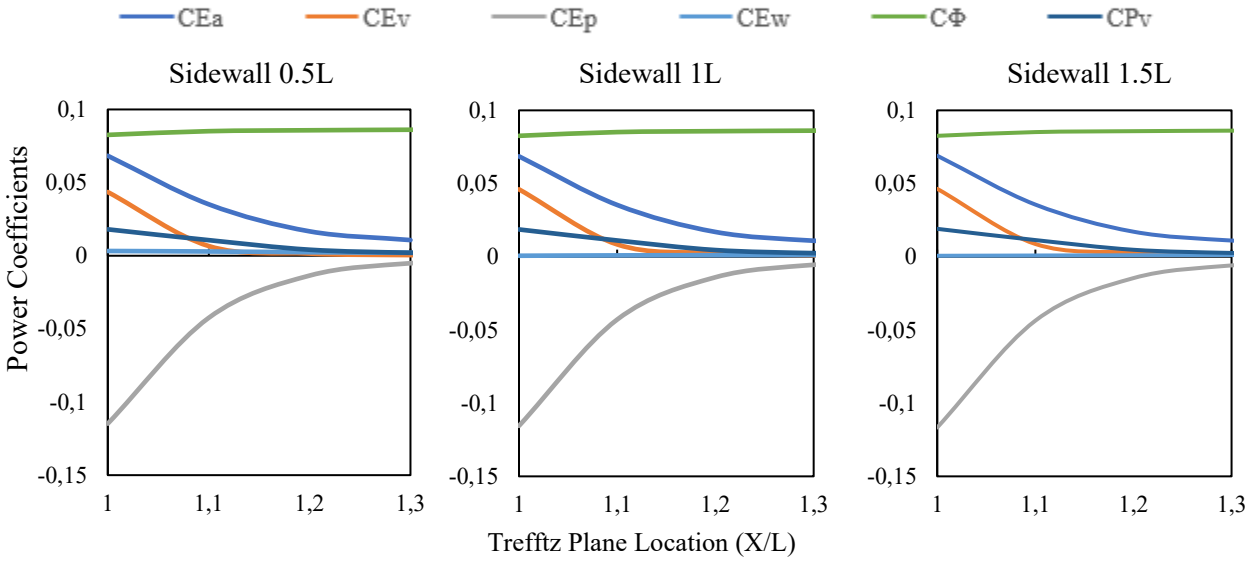

Fig. 16: Power Balance coefficients development with change in Trefftz plane location and side surface distance ($0.5L$, $1L$ and $1.5L$).

Drela [4] assumes P_V is negligible, unless heat is added and the pressure is far different from the ambient pressure. However, in this case, the results show CP_V is nonzero. Sanders and Laskaridis [8] showed when P_V is used with a defined control volume where the Trefftz plane is located at the aftbody for instance, it contains a large isentropic contribution that will exchange with the total energy rate as the Trefftz plane gets moved further downstream. CP_V has a dissipative component and one which will return to a free-stream state isentropically. There is currently no method to split these two components locally. Integrating this term over the whole domain cancels out the isentropic contribution but still leaves a residual dissipative amount behind. These dissipative residual results that CP_V is never zero at any given Trefftz plane location but reaches a constant value at a certain Trefftz plane location downstream of the body. The results of CP_V dissipative residual creates a divergence of 1.3% in volumetric drag coefficient values gained from using the PBM and CFD volume-based drag coefficient as seen in Fig. 17.

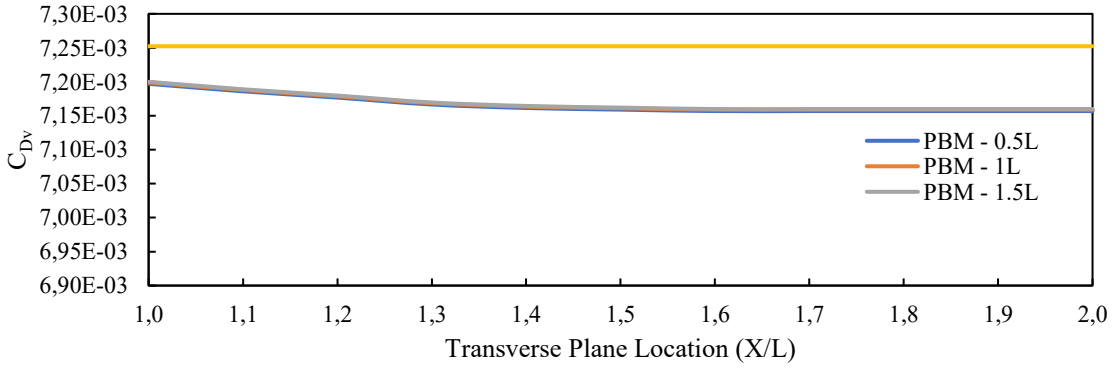

Fig. 17: Power Balance volume-based drag coefficient compared to conventional volume-based drag coefficient prediction as the Trefftz plane moves downstream in the wake.

Fig. 18 shows the plots of the PER, EWC and revised EWC with the change of control volume side surfaces and Trefftz plane location. This is because EWC uses the total energy rate ($\dot{\varepsilon}$) without incorporating volumetric mechanical power CP_V. For incompressible cases, CP_V is zero, having no influence on the PBM coefficient and value as the Trefftz plane is moved downstream. Due to the energy exchange problem of CP_V it is better to rely on dissipation which is locally fully dissipative. Based on this concept Sanders and Laskaridis [8] used an equation known as the potential for energy recovery (PER) as a performance metric. The revised EWC and PER performance parameters show a good correlation between values at the trailing edge but increasingly deviate from each other at X/L = 1.1. The large deviation of the PER ~ $0.5L$ value is due to the previously mentioned phenomenon that $\dot{E}_\omega$ is non-zero at the aftbody which means that $\dot{E}_\omega$ has not converted all of its energy into $\dot{E}_a$ and $\dot{E}_v$ which lowers the PER rating.

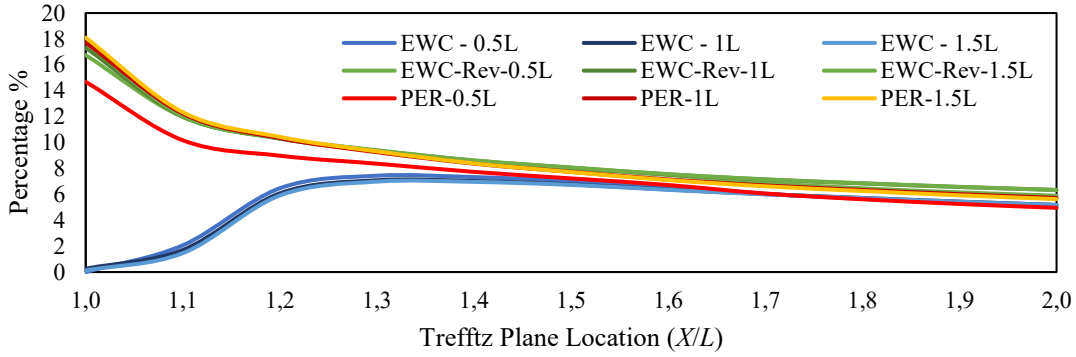

Fig. 18: Recoverable energy percentage using multiple performance parameters.

VII. Conclusion

RANS validation of the CFD method was performed using a 2D RAE2822 transonic airfoil and two bodies (F-57 and MBB shape 3), one for incompressible flow, and the other for transonic compressible flow. It was concluded that a polyhedral mesh paired with SST *k-ω* turbulence model amongst all tested RANS turbulence models, gave the most accurate results compared to experimental results. The PBM and PER was used in a validation case for the incompressible F-57 low drag body and then implemented on compressible MBB shape 3. The far field PBM drag coefficient compared well to momentum-based near field drag coefficient for subsonic flow conditions but showed increasing deviation values for compressible flow conditions due to CP_V having a dissipative component and one which will return to a free-stream state isentropically that by integrating CP_V over the whole domain cancels out the isentropic contribution but still leaves a local residual dissipative amount behind. While using the PER metric showed that most recoverable energy can be captured at the aft portion of a fuselage.

For further studies, a multi-objective optimization study based on the PARSEC construction method for a 3D fuselage shape can incorporate PBM to be used for either results analysis or can be used as a driving optimization objective.

Acknowledgments

The author would like to thank the South African National Research Foundation for its financial support.

References

[1] Huyssen, R. J., Spedding, G. R., Mathews, E. H., & Liebenberg, L. (2012). Wing-body circulation control by means of a fuselage trailing-edge. *Journal of Aircraft. 49(5)*, pp. 1279-1289.

[2] Smith, L., Craig, K. J., Meyer, J. P., & Spedding, G. R. (2017). Modifying low-drag bodies to generate lift: a computational study. *Journal of Aircraft, 54(3)*, pp. 1150-1161.

[3] Smith, L., Craig, K. J., Meyer, J. P., & Spedding, G. R. (2019). Numerical investigation of the aerodynamic performance for an alternative wing–body–tail configuration. *Journal of Aircraft, 56(1)*, pp. 250-261.

[4] Drela, M. (2009). Power balance in aerodynamic flows. *AIAA Journal, 47(7)*, pp. 1761-1771.

[5] Mutangara, N. E., Smith, L., Craig, K. J., & Sanders, D. S. (2021). Potential for Energy Recovery of Unpowered Configurations Using Power Balance Method Computations. *Journal of Aircraft, 58(6)*, pp. 1364 - 1374.

[6] Fernández, A.M. and Smith, H., (2020). Effect of a fuselage boundary layer ingesting propulsor on airframe forces and moments. *Aerospace Science and Technology*, *100*, 105808.

[7] Lv, Peijian, Defu Lin, and Li Mo. (2022). A Power Based Analysis for a Transonic Transport Aircraft Configuration through 3D RANS Simulations, *Applied Sciences*, *12(20):* 10194.

[8] Sanders, D. S., & Laskaridis, P. (2020). Full-Aircraft Energy-Based Force Decomposition Applied to Boundary-Layer Ingestion. *AIAA Journal, 58(10)*, pp. 4357-4373.

[9] Sato, S. (2012). *The power balance method for aerodynamic performance assessment.* Doctoral dissertation, Massachusetts Institute of Technology.

[10] Reist, T. A., & Zingg, D. (2017). High-fidelity aerodynamic shape optimisation of a lifting-fuselage concept for regional aircraft. *Journal of Aircraft, 54(3)*, pp.1085-1097.

[11] Ciliberti, D., De Luca, L., & Nicolosi, F. (2016). *An improved preliminary design methodology for aircraft directional stability prediction and vertical tailplane sizing.* Naple: Doctoral dissertation, Universita Degli Studi Di Napoli "Federico II".

[12] Drela, M. (2010). *TASOPT 2.0.* Tech. rep., Massachusetts Institute of Technology.

[13] Odendaal, D., Smith, L., Craig, K.J., Mutangara, N.E. & Sanders, D. (2023). Fuselage Optimization Study for Improved Recoverable Energy, Unpublished.

[14] Cook, P. H., McDonald, M. A., & Firmin, M. C. (1979). Aerofoil RAE 2822 - Pressure distributions, and boundary layer and wake measurements. *Experimental Data Base for Computer Program Assessment*, AGARD Report AR, 138.

[

[16] Koti, D., & Ayesha Khan, M. (2018). Numerical Analysis of Transonic Airfoil. *International Journal of Engineering Research & Technology (IJERT), 7(05)*, pp. 132-135.

[17] Roache, P. J. (1994). Perspective: A method for uniform reporting of grid refinement studies. *Journal of Fluids Engineering, Transactions of the ASME, 116(3)*, pp. 403-413.

[18] Slater, J. W. (2002, February 10). *RAE2822 Transonic Airfoil*. Retrieved from NPARC Alliance Validation Archive: https://www.grc.nasa.gov/www/wind/valid/raetaf/raetaf.html

[19] Gao, B., Qu, Q., & Agarwal, R. K. (2018). Aerodynamics of a transonic airfoil above wavy ground. *2018 AIAA Aerospace Sciences Meeting*, SciTech Forum, AIAA 2018-1784, Kissimmee, Florida, 8-12 January.

[20] Swanson, R. C., & Rossow, C.-C. (2011). An efficient solver for the RANS equations and a one-equation turbulence model. *Computers & Fluids, 42(1)*, pp. 13-25.

[21] Hirschel, E. H. (1989). *Finite approximations in fluid mechanics II: DFG priority research program, results 1986–1988.* Braunschweig, Germany, Wiesbaden, Germany: Friedr. Vieweg.

[22] Della Vecchia, P., Daniele, E., & D'Amato, E. (2014). An airfoil shape optimisation technique coupling PARSEC parameterisation and evolutionary algorithm. *Aerospace Science and Technology, 32(1)*, pp. 103-110.

[23] Shahrokhi, A., & Jahangirian, A. (2007). An efficient aerodynamic optimisation method using a genetic algorithm and a surrogate model. *16th Australasian Fluid Mechanics Conference*, pp. 475-480, Austria.

[24] Lorenz-Meyer, W., & Auleha, F. (1979). *Experimental data base for computer programme assessment: MBB - Body Of Revolution NO. 3.* Report of the fluid dynamics panel working Group 04, AGARD Advisory Report No. 138.

[25] Patel, V. C., Lee, Y. T., & Güven, O. (1974). Measurements in the thick axisymmetric turbulent boundary layer and the near wake of a low-drag body of revolution In Turbulent Shear Flows I 1979. *In Turbulent Shear Flows I 1979*, pp. 137-153.

[26] Wang, Y., Zhang, Y., Li, S., & Meng, D. (2015). Calibration of a γ-Reθ transition model and its validation in low-speed flows with high-order numerical method. *Chinese Journal of Aeronautics, 28(3)*, pp. 704-711.

[27] Chase, N., Rademacher, M., Goodman, E., Averill, R., & Sidhu, R. (2010). A benchmark study of optimisation search algorithms. *Red Cedar Technology, MI, USA*, pp. 1-15.

[28] Lamprakis, I. Sanders, D. S., & Laskaridis, P (2023). Fundamental Concepts of Boundary Layer Ingestion Propulsion, Unpublished

2023-01-19

Validation case studies of a numerical approach towards optimization of novel fuselage geometries

Odendaal, Diwan U.

AIAA

Odendaal DU, Craig KJ, Smith L, et al., (2023) Validation case studies of a numerical approach towards optimization of novel fuselage geometries. In: AIAA SciTech Forum 2023, 23-27 January 2023, National Harbor, Maryland, USA

https://doi.org/10.2514/6.2023-1555